Chemical Geology 355 (2013) 1–12

Contents lists available at ScienceDirect

Chemical Geology

journal homepage: www.elsevier.com/locate/chemgeo

Disturbance to the $^{40}Ar/^{39}Ar$ system in feldspars by electron and ion beam irradiation

S. Flude [a,*], S.C. Sherlock [a], M.R. Lee [b], S.P. Kelley [a]

[a] CEPSAR (Centre for Earth and Planetary Space and Astronomical Research), The Open University, Walton Hall, Milton Keynes MK7 6AA, UK
[b] School of Geographical and Earth Sciences, University of Glasgow, Gregory Building, Lilybank Gardens, Glasgow G12 8QQ, UK

ARTICLE INFO

Article history:
Received 5 November 2012
Received in revised form 4 July 2013
Accepted 5 July 2013
Available online 13 July 2013

Editor: K. Mezger

Keywords:
$^{40}Ar/^{39}Ar$ dating
Electron irradiation
Thermochronology
Electron microscopy

ABSTRACT

The extent to which intracrystalline microtextures influence the diffusion of radiogenic Ar within alkali feldspars from slowly cooled igneous rocks is a long standing question in thermochronology. By combining high-resolution electron microscopy with *in-situ* UV-laser ablation microprobe $^{40}Ar/^{39}Ar$ analysis the interplay of microtextures with isotope ages can be studied directly, enabling some of the assumptions underlying $^{40}Ar/^{39}Ar$ thermochronological techniques to be tested and allowing deduction of thermochronological and geological histories. However, there are numerous potential mechanisms by which a sample can be damaged and its Ar-isotope system disturbed by such microscopy techniques. To test this hypothesis, perthitic alkali feldspars from the 270–280 Ma Dartmoor Granite, UK, and gem-quality orthoclase from Itrongay, Madagascar (~470 Ma) were polished with colloidal silica or etched with hydrofluoric acid and irradiated with electrons and Ga^+ ions. The accelerating voltages and currents used were typical of those for electron beam imaging by scanning electron microscopy, X-ray analysis and mapping by electron probe, and for extraction of foils using the focused ion beam technique. No disturbance to the Ar-isotope system was observed for Ga^+ ion irradiation, or for low-resolution SEM imaging, but electron irradiation of small areas for long durations, as occurs during extended high-magnification SEM imaging, was found to disturb the Ar-isotope system over hundreds of micrometre sized areas by the addition of K and atmospheric Ar, producing anomalously young apparent $^{40}Ar/^{39}Ar$ ages. The best explanation for this age disturbance is electromigration of K and implantation of atmospheric Ar during sample charging.

1. Introduction

Alkali feldspars are abundant in the continental crust, and being rich in K they are used extensively for radiometric dating by the K/Ar or $^{40}Ar/^{39}Ar$ methods. The microstructures of alkali feldspars are considered to affect the intracrystalline diffusion of radiogenic Ar (Parsons et al., 1988), and this phenomenon has been exploited to deduce complete thermal histories of samples using the multi-domain diffusion (MDD) model (Lovera et al., 1989; Richter et al., 1991). However, the degree and nature of the impact of microtextures on Ar-diffusion is variable within and between individual crystals (*e.g.* Parsons et al., 1988, 1999), and this, combined with the increasing recognition of multiple generations of K-feldspar within a single grain (*i.e.* multiple discrete crystallisation events — *e.g.* Harrison et al., 2010; Villa and Hanchar, 2013; Villa, 2006; Villa et al., 2006) may be the reason why only ~50% of MDD studies produce geologically meaningful results (Lovera et al., 2002).

In an attempt to better understand the influence of microtextures on the distribution of Ar within alkali feldspars, several studies have combined SEM imaging with laser ablation microprobe (UV-LAMP) $^{40}Ar/^{39}Ar$ analysis and, sometimes, furnace cycle heating experiments on the same sample (Reddy et al., 1999, 2001; McLaren and Reddy, 2008). Some of these investigations have provided surprising results, for example the discovery of concentric age variations reminiscent of a cooling profile within a microtexturally complex detrital grain from a sedimentary rock (Reddy et al., 2001). In these studies various electron beam techniques have been used to characterise a sample that was later irradiated for $^{40}Ar/^{39}Ar$ analysis. There has been a tacit assumption that interaction of the electron beam with the sample does not affect the siting or distribution of Ar or K atoms. However, the common understanding of SEM and electron microprobe (EMPA) users is that both amorphous and crystalline samples may be damaged by the electron beam, particularly in relation to their alkali content (Sweatman and Long, 1969). Therefore we have reviewed the mechanisms by which the $^{40}Ar/^{39}Ar$ system in alkali feldspars may be disturbed during electron irradiation and have sought to assess their impact on the $^{40}Ar/^{39}Ar$ system by coupled electron imaging and $^{40}Ar/^{39}Ar$ analysis

* Corresponding author.
E-mail address: flude@ruc.dk (S. Flude).

0009-2541
http://dx.doi.org/10.1016/j.chemgeo.2013.07.003

of alkali feldspars from the 270–280 Ma Dartmoor Granite (UK) (Chesley et al., 1993) and the ~470 Ma gem quality Itrongay orthoclase from Madagascar (Arnaud and Kelley, 1997; Wartho et al., 1999; Nägler and Villa, 2000; Flude et al., Under review). We have also examined the effect of ion irradiation on the $^{40}Ar/^{39}Ar$ system since focussed ion beam (FIB) milling is being increasingly commonly used to extract foils from feldspar grains for microtexture characterisation by transmission electron microscopy (TEM) (*e.g.* Lee, 2010) and the small extent of sample damage produced by FIB milling makes FIB-TEM characterised samples a good candidate for additional *in-situ* UV-LAMP $^{40}Ar/^{39}Ar$ studies. As will be shown, there are numerous mechanisms by which electron- and ion-beam techniques can damage, transform or contaminate alkali feldspars, and so render them unsuitable for subsequent $^{40}Ar/^{39}Ar$ dating studies. Furthermore, we note that the degree of damage may vary with the coarseness and spatial distribution of Ab- and Or-rich phases and the coherency of the microtextures, and so our experimental programme has used two alkali feldspars with very different microtextures.

2. Potential mechanisms of damage in SEM analysis and FIB milling

Damage to an alkali feldspar during electron irradiation is manifested by a decay in the intensities of X-ray emission from alkali metals during EMPA (*e.g.* Gedeon et al., 2008). Most studies of this phenomenon have used samples of glass or halide salts, where the effect is most pronounced owing to the relatively weak bonding of alkali ions in the glass structure and greater proportion of non-bridging oxygens (Spray and Rae, 1995). During electron irradiation, alkalis become separated from their bridging O; the O^- ions migrate to the surface of the sample where they can accumulate to form a bubble beneath the carbon-coating (Lineweaver, 1963; Nielsen and Sigurdsson, 1981). With continued irradiation, the sample is heated and a localised electric field develops, promoting the diffusion of positively charged alkali ions, although the relative contributions of charging and thermal effects in diffusion remain unclear (Gedeon et al., 1999; Gedeon and Liška, 2001; Jiang and Silcox, 2002). While moderate electron beam conditions and use of a carbon-coating on the sample are routinely employed to minimise sample charging and damage, these precautions do not necessarily completely prevent charging in insulating samples such as silicate materials. The redistribution of alkalis within feldspar crystals during electron irradiation has been reported (Autefage, 1980). The degree to which alkalis are lost through this electromigration depends on the depth of this negatively charged area within the sample; if it occurs close to the surface, alkalis are more likely to escape (Gedeon et al., 2008). However there is a consensus that the decay in X-ray intensity during EMPA is due to migration of alkali ions into the bulk of the sample beyond the information depth (*e.g.* Cazaux, 1986).

In a K-bearing crystal, radiogenic Ar occupies the site of its parent K atom but, unlike the remaining K atoms, it is not bonded; thus Ar might be more mobile than alkalis during electron irradiation, despite the lower probability of it forming an ion. Materials containing high concentrations of O or halides may be affected by O or halide desorption. This may occur by the Auger process: halide or O atoms are ionised when they interact with an electron and during the de-exciting process lose two electrons. This process leads to the formation of neutral O species, or positively charged halides, which are thus unavailable for ionic bonding (Cazaux, 1996). In poorly conducting specimens the electrical charges are restored slowly, which may result in loss from the sample of O or halides (Cazaux, 1996). This presumably causes a (highly localised) breakdown of the crystal lattice and may result in Ar-loss or breaking of bonds to alkali ions, allowing them to be more easily redistributed by electromigration.

The mechanisms for sample damage by electron irradiation thus far described are dominated by the development of an electrical field which promotes charging and debonding of alkalis. However, McConnell (1969) documented ionisation-induced sample damage and reaction to form an amorphous product in microperthitic alkali feldspar using an electron microscope operating at 100 keV with a current of 0.02 μA and a spot size of 1.25 μm. The amorphous material was microporous and he found that coarser Ab-rich exsolution lamellae damaged more readily than their host Or-rich component. This greater susceptibility to damage may not only be due to the greater mobility of Na over K, but may also relate to the concentration of misfit dislocations on the boundaries of coarse Ab-rich exsolution lamellae (*e.g.* Lee et al., 1995 — Shap granite). While the operating conditions employed by McConnell are different to those for routine SEM or EMPA work, the study highlighted the control on sample damage that is exerted by pre-existing microtextures. We also note that most studies into the electromigratory effects in alkali-bearing samples are carried out using samples coated with carbon which is then grounded (Gedeon et al., 1999, 2008, 2009; Jurek and Gedeon, 2008). However, for the imaging techniques best suited to revealing feldspar microtextures, such as charge contrast (CC) imaging (Flude et al., 2012), orientation contrast (OC) imaging (Reddy et al., 1999, 2001) and electron backscattered diffraction (EBSD) (Prior et al., 1999; McLaren and Reddy, 2008), it is often essential or at least desirable for samples to remain uncoated when analysing feldspars. Therefore the geometry, intensity and dynamics of the electrical field generated during electron irradiation may be different to that on carbon coated samples.

The heating of a sample by an electron beam is known to cause damage and can be particularly problematic for production of high-resolution EBSD maps whereby sequential spots are closely spaced. The temperature rise (ΔT) within a material as a consequence of its interaction with an electron beam can be estimated by $\Delta T = 4.8E_0\, i\, /\, (kd)$ (Reed, 2005). E_0 is the incident electron energy (keV), i is the current (μA), k is the thermal conductivity of the sample (W m^{-1} K^{-1}) and d is the beam diameter (μm). Assuming an accelerating voltage of 25 keV, a current of 50 nA, a beam diameter of 2 μm and a maximum sample thermal conductivity of 1.5 W m^{-1} K^{-1} (Smith and Brown, 1988), an alkali feldspar crystal may experience an increase in temperature of 200 K (Fig. 1B). While various studies have determined the thermal conductivities of alkali feldspars to be 1.5–2.9 W m^{-1} K^{-1} (Sass, 1965; Höfer and Schilling, 2002; Pertermann et al., 2007), Cahill et al. (1992) calculated minimum thermal conductivities for feldspars of 0.98 W m^{-1} K^{-1} at 300 K. Samples with this thermal conductivity under the above conditions could expect a temperature rise of 306 K (Fig. 1B). The fractional loss of $^{40}Ar^*$ from a feldspar due to heating can be calculated for a given grain size (McDougall and Harrison, 1999): Fig. 1C shows the fractional loss of Ar that would be experienced by a range of grain sizes resulting from 8 min (a relatively long imaging time) at the range of temperatures a feldspar sample could be expected to experience during electron irradiation. Small diffusion domains of 1 μm radius would only lose less than 1% of their radiogenic ^{40}Ar ($^{40}Ar^*$), even when analysed at high current (100 nA–500 °C) and assuming a low sample conductivity. A 306 °C rise in temperature would only result in significant (>5%) Ar-loss from grains less than 30 nm in diameter and, as this grain size is smaller than the recoil distances for ^{39}Ar during neutron irradiation (~0.3 μm total depletion layer thickness and 0.7 μm partial depletion layer thickness, Jourdan et al., 2007), such grains or diffusion domains are already unsuitable for *in-situ* laser ablation $^{40}Ar/^{39}Ar$ dating. Sample heating during electron irradiation is unlikely to cause diffusional loss of radiogenic $^{40}Ar^*$, but movement of K within the sample by electromigration may be enhanced by elevated temperatures in the sample–electron interaction volume (Spray and Rae, 1995).

Samples may also become contaminated with hydrocarbons during SEM analysis. Hydrocarbon molecules present in the microscope chamber or on the sample surface may be polymerised when they interact with electrons, becoming immobilised on the sample surface in a form that is resistant to chemical etching (Egerton et al., 2004). This process may be particularly problematic for subsequent $^{40}Ar/^{39}Ar$ analysis as

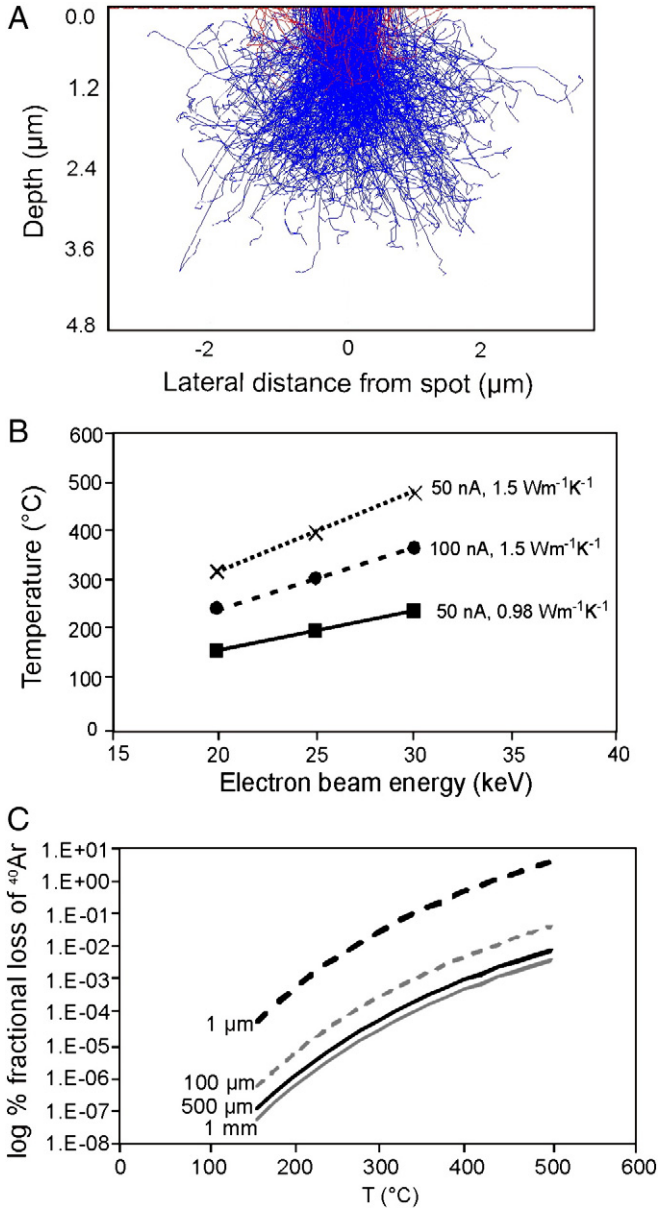

Fig. 1. A: Monte Carlo simulation of electron trajectories during electron irradiation for SEM or EMPA analysis, using CASINO ("monte CArlo SImulation of electroN trajectory in sOlids", http://www.gel.usherbrooke.ca/casino/). Electrons are modelled to penetrate to between 3 and 4 μm into the sample. 1000 electron trajectories modelled at 20 keV assuming a sample composition of $KAlSi_3O_8$ and a density of 2.55 g cm^{-3}. B: Calculated temperature rise with electron beam energy in a sample of orthoclase feldspar during 8 min of sample irradiation, assuming different beam currents and sample conductivities. With such conditions, a temperature rise of between 160 and 480 °C could be expected. C: Fractional loss of $^{40}Ar^*$ that could be expected, for different diffusion domain sizes, based on 8 min of elevated temperature during electron beam irradiation. Even diffusion domains as small as 1 μm diameter only experience a loss of ~1% $^{40}Ar^*$ at the highest likely temperatures.

hydrocarbon fragments with masses 36, 37, 38, 39 and 40 may cause interferences within the mass spectrometer. While most mass spectrometers are able to resolve the subtle mass differences between Ar-isotopes and contaminants for masses 37–40, few noble gas mass spectrometers are as yet able to discriminate between ^{36}Ar and hydrocarbon or Cl contaminants. ^{36}Ar is used to correct for atmospheric ^{40}Ar with the assumption that $^{40}Ar/^{36}Ar = 298.56$ (Lee et al., 2006), thus relatively small inaccuracies in the measured ^{36}Ar content may result in relatively large inaccuracies on the final $^{40}Ar/^{39}Ar$ age. For example, an analysis acquired during the present study gives an age of 271 Ma with a low-moderate ^{36}Ar yield (10 counts, blank corrected), but would have an apparent age of 256 Ma if the apparent ^{36}Ar yield is increased by a factor of 3 (*i.e.* $^{36}Ar = 30$ counts).

Some SEM techniques, such as electron backscatter diffraction (EBSD) or charge contrast imaging (CCI) require prior chemical–mechanical polishing of the sample surface to be studied with colloidal silica. This process removes the upper, mechanically damaged layer produced by standard polishing techniques. However, some geological materials, particularly some alkali feldspars, may rapidly dissolve in the colloidal silica solution (Prior et al., 1999). This process may result in selective removal or redistribution of K and Ar within the sample.

FIB milling is commonly used to prepare electron-transparent specimens for TEM imaging, and is being increasingly used to study geological materials, including alkali feldspars (Smith et al., 2006; Lee et al., 2007; Mark et al., 2008). Milling uses ~30 keV Ga^+ ions to excavate trenches in a sample, leaving a cross-sectional foil of around 20 × 10 μm, which is lifted out and further thinned to an appropriate thickness. Samples are often coated with C or Au to prevent charging and a strip of Pt is deposited over the area of interest to prevent the foil from being damaged by the ion beam. Such ion damage ranges from the generation of extensive lattice defects to complete amorphization of the material (Prenitzer et al., 2003). Both of these processes may affect the siting and retention of Ar or K. Additionally, local temperature rises of up to 1000 °C have been documented during Ga^+ irradiation (Prenitzer et al., 2003), 30 min of which may cause minor (2%) diffusive Ar-loss in diffusion domains of up to 1 mm radius, and complete degassing of domains less than 10 μm radius. Furthermore, the Pt layer is deposited by decomposition of an organic Pt-gas (trimethyl platinum) in the ion beam (Wirth, 2009); this may result in greater degrees of contamination by hydrocarbons, as described above.

3. Samples and methodology

Alkali feldspars from slowly cooled igneous rocks are typically composed of a mosaic of regions that are both pristine and have been deuterically altered, giving a heterogeneous distribution of micropores and dislocations, and a wide range of diffusion domain sizes. The presence of these microtextures may mean that different parts of the grain yield contrasting $^{40}Ar/^{39}Ar$ ages (*e.g.* Parsons et al., 1988, 1999; Reddy et al., 1999; McLaren et al., 2007). Many of the potential damage mechanisms described above involve loss or redistribution of K and Ar by diffusion or migration. As a result, samples containing smaller diffusion domains with respect to K or Ar are likely to experience greater disturbance than those with larger domains. For this reason, samples of two alkali feldspars that differ in bulk chemical composition, mineralogy and microtexture were used to quantitatively assess the impact on the Ar system of electron and ion irradiation during SEM and FIB milling.

Sample MAD is a gem quality alkali feldspar from Itrongay, Madagascar. It is a transparent, chemically homogenous, microtexturally simple tweed orthoclase with 1.2% total FeO, which gives it a characteristic yellow colour (Wartho et al., 1999) and has produced $^{40}Ar/^{39}Ar$ ages of 435 ± 8 Ma (Arnaud and Kelley, 1997), 461 ± 6 Ma (Nägler and Villa, 2000) and 416–474 (Flude et al., under review). The latter study, which was carried out contemporaneously with the present investigation, revealed large (cm-scale) age gradients within the Itrongay feldspar which were interpreted as diffusion profiles, confirming previous conclusions that Ar release from this feldspar is controlled by thermally-activated volume diffusion from a single diffusional domain that equates to the grain size (Arnaud and Kelley, 1997; Wartho et al., 1999). In the context of the present study, sample MAD represents the microtexturally simpler of the two alkali feldspars. We hypothesise therefore that owing to its lack of subgrains and very low density of dislocations it is less likely to experience significant damage during electron imaging, Ga^+ radiation, etching or chemical polishing. At the start of the present study it was assumed that the homogeneity of Itrongay feldspar would mean that any variation in $^{40}Ar/^{39}Ar$ age

recorded would be attributable to sample damage by SEM, FIB, polishing and etching. However, the large, natural systematic age variations that were discovered by Flude et al. (under review) have rendered much of the data from the MAD sample inappropriate for the present study. Nevertheless, a small data set from the MAD samples are presented here to allow comparison of the ^{36}Ar abundances and Cl and hydrocarbon contamination between samples and allow qualitative assessment of any age variation observed.

Sample SW14 is from the Dartmoor Granite, SW England. Dartmoor feldspars are microstructurally complex, containing micro- and cryptoperthites, patch and vein perthites, including intergrowths of orthoclase and microcline, and microcline veining (Flude et al., 2012). SEM imaging (backscattered electrons (BSE) and charge contrast (CC) imaging) from the present study and currently unpublished observations show that alkali feldspars in the groundmass of the Dartmoor Granite contain pristine cryptoperthites and microperthites along with patch microperthites, but the microcline veins that occur in some phenocrysts (Flude et al., 2012) have not been observed. BSE images of sample SW14 and their interpretation are shown in Fig. 2. Fig. 3 shows detailed BSE and CC images that are representative of deuteric and pristine areas of SW14 groundmass feldspars. The groundmass alkali feldspars give relatively consistent $^{40}Ar/^{39}Ar$ ages of

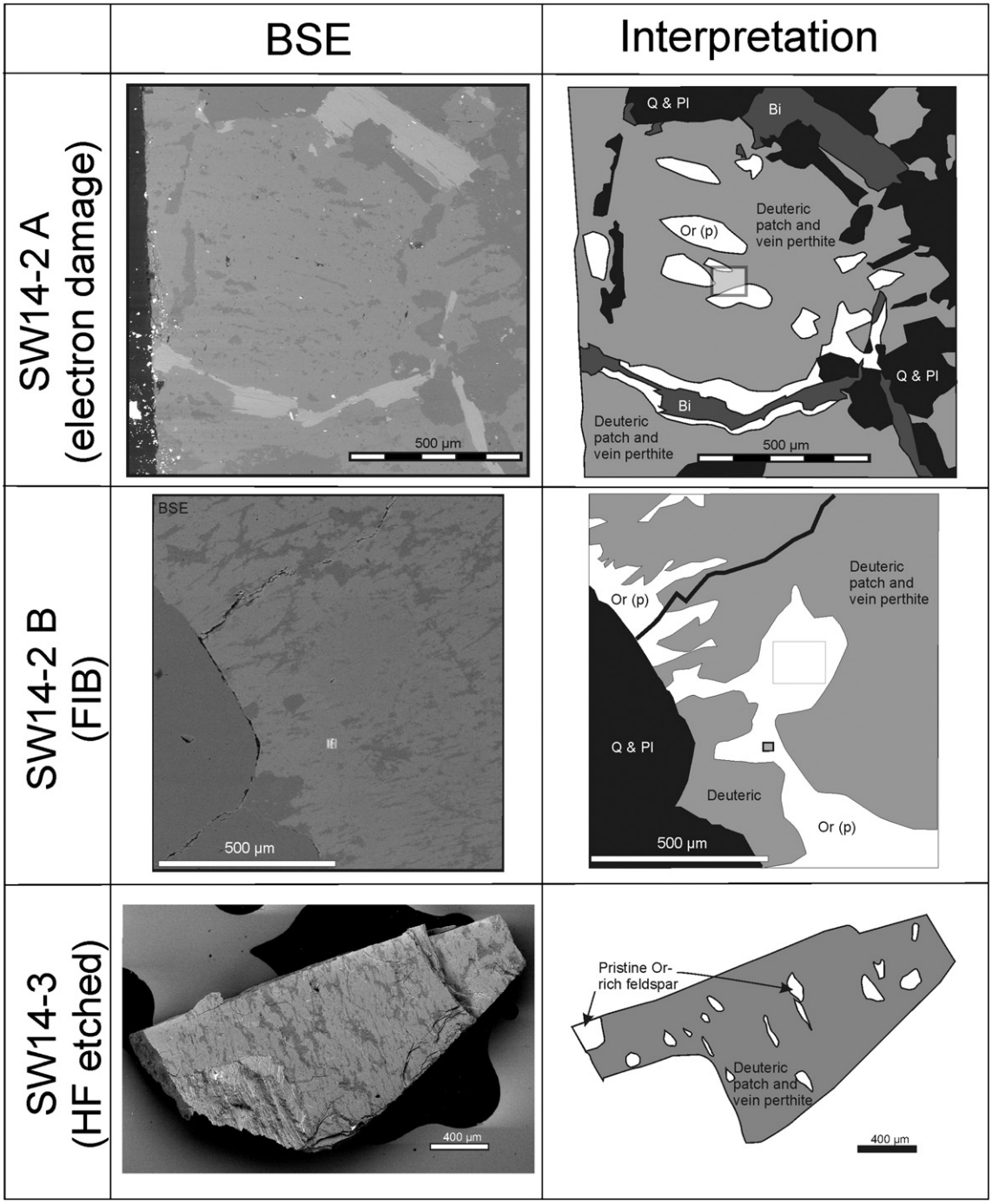

Fig. 2. SEM-BSE images and simplified textural interpretation of the SW14 sub samples. On SW14-2B the FIB pit is visible on the BSE image as a small white square. The larger square on the interpretation of SW14-2B represents an area that was imaged at high magnification and was observed with CC imaging to have retained negative charge. The square on SW14-2A represents the area of electron-beam damage from imaging the sample at high magnification for 8 min. Q = quartz, Pl = plagioclase feldspar, Bi = biotite mica, Or (p) = pristine orthoclase feldspar (crypto- or microperthitic).

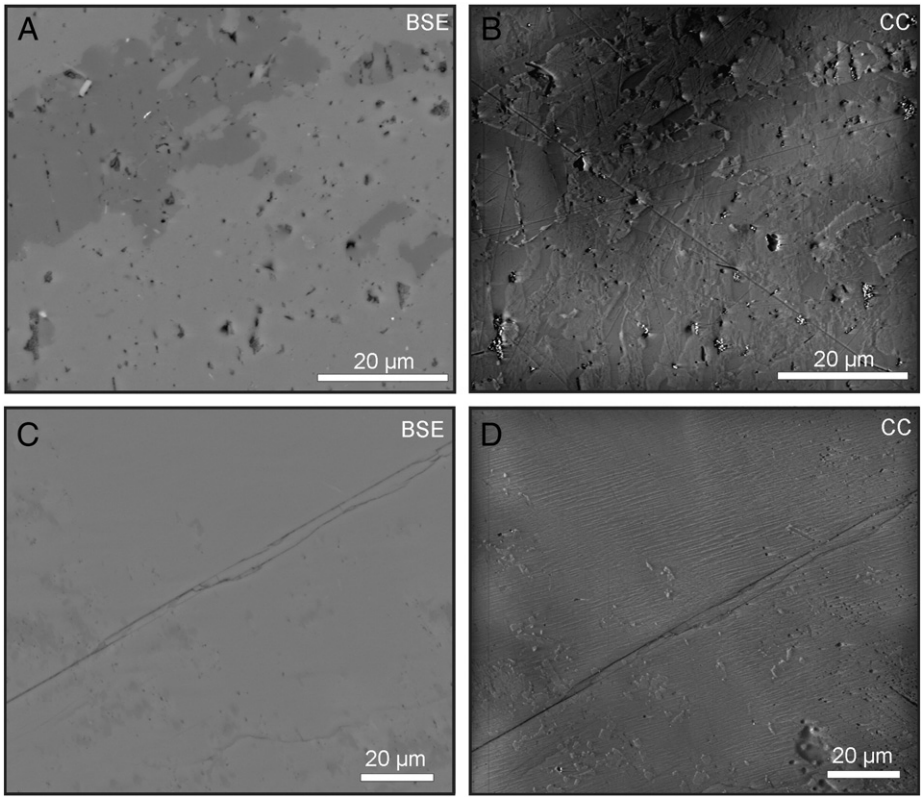

Fig. 3. Representative BSE and CC images of end-member feldspar microtextures observed in groundmass Dartmoor feldspars. Images (A) and (B) are BSE and CC images of the same field of view illustrating a deuteric patch perthite. Dark grey areas in BSE are the Ab-rich phase while lighter grey areas are the Or-rich phase. Micropores are abundant and the CC image reveals that both the Ab-rich and Or-rich phases appear to be formed from many subgrains. Images (C) and (D) are BSE and CC images of the same field of view illustrating an area composed predominantly of pristine Or-rich feldspar. Small patches of Ab-rich feldspar can be seen in the BSE image, but the majority of the field of view is formed by homogenous, pore-free Or-rich feldspar. The CC image reveals a cryptoperthite containing numerous high-contrast Ab-rich lamellae (Flude et al., 2012).

260–280 Ma (1 σ age errors on individual spot analyses are typically 0.5–1.5% — *i.e.* 2–4 Ma) and show no systematic core-rim, or any internal linear age variations (this study and unpublished data by Flude). This lack of systematic intragranular age variation suggests that the microstructures of Dartmoor feldspars form diffusion domain boundaries of different sizes (thus with different closure temperatures and resulting $^{40}Ar/^{39}Ar$-ages) with diameters equal to or less than the laser-ablation spot size (~100 μm). Therefore if any cooling profiles are present in these feldspars they are below the resolution of the laser ablation technique. As such, no systematic age variation is expected to occur naturally in this sample so any systematic spatial variation in age or $^{40}Ar/^{39}Ar$ values identified within an electron-irradiated crystal may be an artefact of the irradiation process.

For each sample (SW14 and MAD), two 300 μm thick, polished slabs (1, 2) and a cleavage fragment (3) were prepared. A flow chart summarising the preparation and analytical procedures for the different sample slabs and fragments is given in Supplementary Fig. 1. All feldspars analysed from SW14 are from the coarse grained (0.5–2 mm) groundmass, rather than phenocrysts. Slab 1 is the control sample and only underwent preparation for $^{40}Ar/^{39}Ar$ analysis. Slab 2 was polished with colloidal silica and imaged using a FEI Quanta field-emission environmental SEM operated at an accelerating voltage of 20 keV prior to irradiation for $^{40}Ar/^{39}Ar$ analysis. These polished slabs were uncoated and imaged at low vacuum (60 Pa, with water vapour in the specimen chamber) by BSE and CC imaging. Selected areas were left under the electron beam at high magnification (4000×, resulting in a scanned area of ~65 × 60 μm) for 8 min (a rather long imaging time that may be relevant for CCI, but less so for BSE, OC and EBSD imaging) to maximise potential sample damage under normal CCI operating conditions. These areas are referred to as "electron damaged" (area included on fragment 2A of each polished slab) and such areas remain visible as a "burn" mark during CC imaging, even after light re-polishing (Flude et al., 2012). High resolution BSE and CC images of the microtextures in these areas were not acquired as the images quickly became dominated by intense charging effects during the irradiation procedure. Slab 2 was then carbon-coated and underwent FIB milling using an FEI Duomill equipped with a field-emission electron gun and ion gun. Platinum was deposited on the sample surface using an electron and ion beam, then pairs of trenches were cut into the sample using 30 keV Ga^+ ions, leaving a ~1 μm thick foil, which was then removed using an *in-situ* micromanipulator. These areas are referred to as "FIB damaged" and are included on fragment 2B. Slab 2 was polished to remove the carbon-coat and the FIB-pits imaged by SEM before being prepared for irradiation for $^{40}Ar/^{39}Ar$ analysis. Cleavage fragment 3 was etched with HF vapour for ~45 s and then imaged in the SEM (BSE and CC), uncoated, using the above conditions. Imaging was carried out at relatively low magnification to minimise damage from charging. Supplementary Fig. 1 summarises the sample preparation and electron/Ga^+ irradiation procedure for the different sample splits.

All polished slabs and cleavage fragments were demounted from their glass slides, washed in acetone and deionised water, broken into fragments approximately 1 cm across, packaged in foil, loaded into a foil tube and irradiated at the McMaster Reactor (Canada) for 33.5 h using cadmium shielding. The neutron flux was monitored using biotite standard GA1550, grains of which were loaded into 1 cm foil packets and distributed throughout the irradiation tube. Grains from each packet were analysed by single grain fusion and J-values for each sample fragment were calculated by linear extrapolation of J-values between standards within the irradiation tube. J-values from each packet were reproducible, suggesting that any horizontal neutron flux variation was minimal so we assume a single J-value for each slab, but note that significant horizontal gradients in neutron flux across the tube may be

under-estimated if the biotite grains were not evenly distributed throughout the packet during irradiation. J-values were calculated assuming an age of 98.79 ±0.96 Ma (Renne et al., 1998). We note the existence of updated ages for GA1550 (Spell and McDougall, 2003; Schwarz and Trieloff, 2007; McDougall and Wellman, 2011), but as this study is investigating the presence or lack of variation within a single sample, calculation of the precise absolute age is unimportant. $^{40}Ar/^{39}Ar$ UV-laser ablation analysis was carried out on all fragments. The distribution of laser spots for each fragment was planned to search for any spatial variation in Ar-age with respect to the areas that had undergone extended electron irradiation or FIB milling. A New Wave Research Ltd LUP 213 nm pulsed Nd-YAG laser was used to ablate pits ~100 μm in diameter across the polished and cleaved surfaces. Unwanted gas species were removed from released gases by two SAES getters, one operating at room temperature and the other at 450 °C, during both the laser ablation (30–60 s) and for an additional 15 s prior to automatic inlet into a Nu Instruments Noblesse mass spectrometer, which is able to resolve ^{36}Ar and $^{36}(C_3)$. Masses 35, and interfering peak shoulders on the high mass sides of masses 36 (36-high) and 39 (39-high) were measured in addition to the Ar isotopes to monitor for Cl and hydrocarbon interferences, respectively. Blanks were measured between each sample analysis. All data were corrected for blanks, ^{37}Ar decay and neutron-induced ^{40}Ar (correction factor $(^{40}Ar/^{39}Ar)_K = 0.0085$); Ca-derived ^{39}Ar and ^{36}Ar were not corrected for due to the very low abundance of Ca in these samples (10 ppm in MAD, (Nägler and Villa, 2000), <0.2 wt.% in SW14 (Flude et al., 2012)) resulting in measured levels of $^{37}Ar_{Ca}$ being indistinguishable from blank. ^{36}Ar yields were variable and a number of spot analyses released such low levels of ^{36}Ar that they are indistinguishable from the blank. During Ar-isotope analysis, no unusual baseline fluctuations were observed and the peak positions for low-abundance isotopes (including ^{36}Ar) were monitored to ensure that the low measured abundances were real and not the result of measuring off-peak. Furthermore, there is no overall correlation between $^{40}Ar/^{39}Ar$ age and ^{36}Ar yield, so the low abundances are not considered to be due to ablating too little material and underestimation of ^{36}Ar. Therefore, these low ^{36}Ar yields are considered to reflect very low ^{36}Ar levels within the sample. Where the ^{36}Ar yields are indistinguishable from or lower than blank (*i.e.* the blank-corrected ^{36}Ar value is zero or negative), it is assumed that the atmospheric Ar content of the analysis is effectively zero and an atmospheric ^{40}Ar correction has not been carried out.

4. Results

Ar-isotope data are given in the Supplementary data set. A summary of the pertinent values is provided in Table 1. Sample SW14-1 (the control Dartmoor feldspar) produced laser-spot $^{40}Ar/^{39}Ar$ ages between 261 ± 2 and 281 ± 3 Ma (1σ errors), as expected and consistent with other dates for the Dartmoor Granite (Chesley et al., 1993). ^{36}Ar abundances were low throughout the sample, with a maximum ^{36}Ar yield of 17 counts above blank (1.87×10^{-14} cm^3 STP), and in many analyses the ^{36}Ar was indistinguishable from blank. By contrast, areas of SW14-2 (the electron-irradiated sample) showed a much greater age range, from 244 to 287 Ma and up to ~200 times greater amounts of ^{36}Ar (up to 206 counts above blank/2.27×10^{-13} cm^3 STP). The etched sample, SW14-3 gave a more constricted age range from 253 to 275 Ma and also produced high ^{36}Ar yields (up to 206 counts above blank/2.27×10^{-13} cm^3 STP). The age ranges for the MAD samples are shown in Table 1, but will not be discussed here as the natural age variability makes comparison of ages inappropriate. The ^{36}Ar values are extremely low for most analyses in all of the sample subsets and are often indistinguishable from blank. Of note is the analysis closest to the centre of electron-beam damage in MAD-2, which has the highest ^{36}Ar value of all MAD analyses (8.9 counts/9.79×10^{-15} cm^3 STP), although we note that this is still lower than the ^{36}Ar abundance in any of the Dartmoor subsamples.

4.1. Hydrocarbon and chlorine contamination

Potential hydrocarbon contamination was monitored by measuring $^{39}(C_3H_3)$ and $^{36}(C_3)$ for both sample and blank (Fig. 4) and abundances are low for all analyses (<~10 counts for $^{36}(C_3)$, <~60 counts for $^{39}(C_3H_3)$). Slightly higher values for $^{39}(C_3H_3)$ were sometimes observed, during both instrument blank and sample analyses, but these were associated with large errors and are, at least in part, an artefact produced by a combination of detector noise and short measurement times on the hydrocarbon peak shoulders. These data points have been retained because the hydrocarbon values are not integral to understanding the Ar-isotope system, and all analyses have been plotted in Fig. 4. The vast majority of the sample analyses are indistinguishable from instrument blank levels at 1 σ and all analyses are indistinguishable at 3σ.

Cl can affect apparent age determinations by causing a $^{1}H^{35}Cl$ interference at mass 36, leading to overestimations of ^{36}Ar, so was monitored by measuring mass 35 for both sample and instrument blank. Most analyses fall in a range between 550 and 800 counts of ^{35}Cl and the sample analyses are indistinguishable from the blanks. The only two data points that appear to have ^{35}Cl greater than blank (both from SW14-2) are associated with large errors and are probably an artefact of short measurement times on the mass 35 peak. The two arrays defined by blank values of ^{35}Cl and ^{36}Ar (Fig. 4) represent the Noblesse background at different times. Any Cl contamination of the sample would be expected to produce a positive correlation between ^{35}Cl and ^{36}Ar. This is not observed (Fig. 4) so we conclude that there is no significant Cl contamination within any of the analysed samples.

4.2. The effect of FIB-milling

The spatial variations in $^{40}Ar/^{39}Ar$-age and ^{36}Ar on SW14-2B, the fragment that underwent FIB-milling, are shown in Figs. 5 and 6. The FIB pit is represented by the small dashed box at the bottom of

Table 1
Summary of pertinent Ar-isotope and age data. Weighted averages and MSWDs are calculated by Isoplot at 95% confidence, using 1σ errors that do not include the error on the J-value. ^{36}Ar values are corrected for blanks and discrimination. "%n <90%" indicated the proportion of the analyses that contain less than 90% radiogenic ^{40}Ar.

Sample	Age				^{36}Ar		$\%^{40}Ar^*$			
	Max.	Min.	Wtd. ave.	MSWD	Max.	Min.	Max.	Min.	%n <90%	n
SW14-1 (Control)	280.7	261.1	274.1 ± 0.9	6.9	17.6	−0.4	100.0	92.5	0	75
SW14-2A (e-damage)	285.9	249.1	271.7 ± 2.8	43	206.1	1.3	99.4	56.7	41	44
SW14-2 B (FIB damage)	285.9	258.7	275.3 ± 2.4	18	16.3	−1.9	100.0	88.3	2	41
SW14-3 (HF-Etch)	274.5	253.4	267.2 ± 1.5	5.4	206.0	3.2	99.1	57.2	17	30
MAD-1 (Control)	456.3	437.6	451.1 ± 2.1	5.9	1.3	−1.2	100.0	99.1	0	21
MAD-2A (e-damage)	465.1	459.3	461.6 ± 1.5	0.47	8.9	0.0	100.0	97.5	0	10
MAD-2B (FIB damage)	451.0	445.2	448.8 ± 1.0	0.85	0.3	−2.8	100.0	99.9	0	9
MAD-3 (HF-Etch)	472.7	468.2	469.8 ± 1.3	0.32	1.7	−0.2	100.0	99.4	0	11

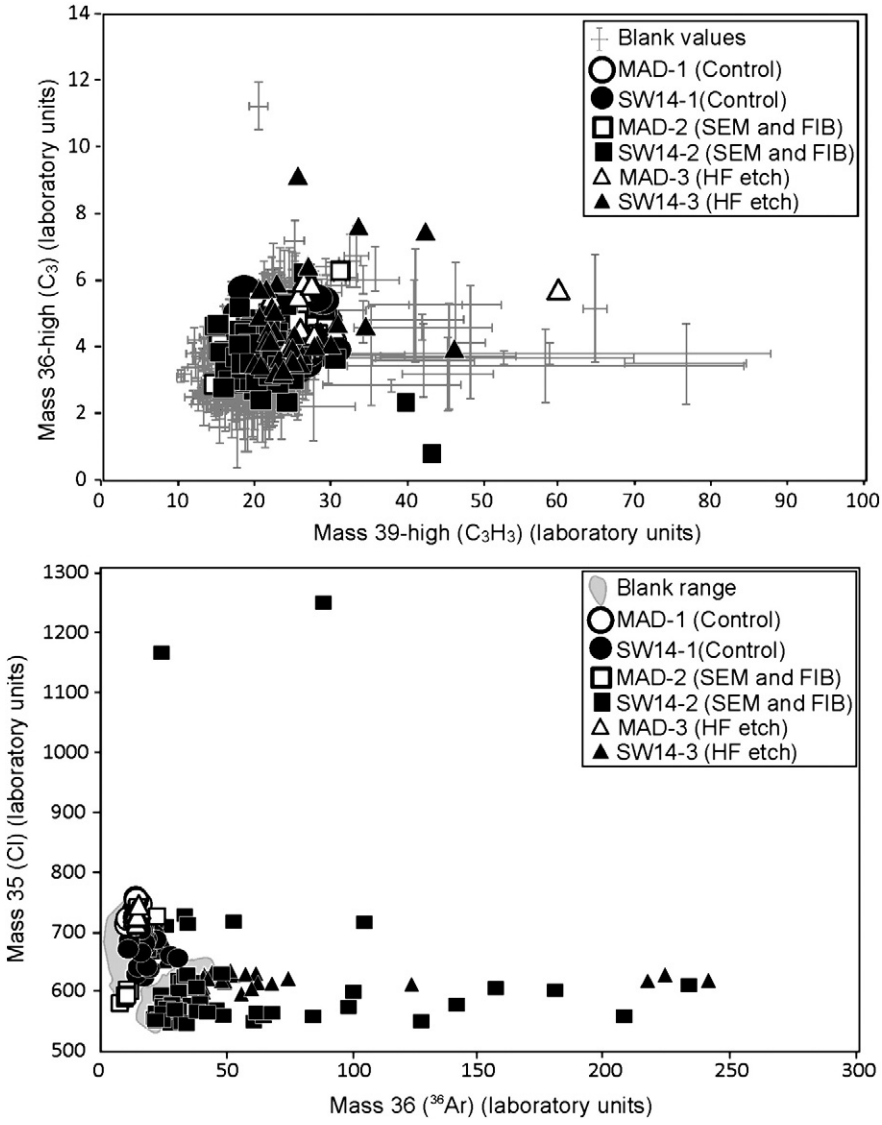

Fig. 4. Measured values of $^{39}(C_3H_3)$, $^{36}(C_3)$, ^{35}Cl and ^{36}Ar for blanks and samples. Error bars for blank analyses are 1 σ. Errors are not shown for sample analyses but in most cases are comparable to the errors on the blank analyses. In most cases, $^{39}(C_3H_3)$, $^{36}(C_3)$ and ^{35}Cl are indistinguishable from blank suggesting that SEM, FIB milling and their various preparation techniques do not introduce significant hydrocarbon or Cl contamination to the sample.

the profile line. The larger dashed box denotes the location of a "burn" mark found during the final stages of CC imaging. This was produced unintentionally during brief imaging of microtextures in the sample. All of the $^{40}Ar/^{39}Ar$ ages and ^{36}Ar yields are within the expected range (as defined by the control slab, SW14-1) and the youngest ages (<265 Ma) tend to be associated with patch perthites, while the larger regions of micro and crypto perthites tend to be associated with the oldest (>280 Ma) $^{40}Ar/^{39}Ar$ ages, as would be expected if feldspar microtexture was the dominant control on diffusion domain size and thus apparent $^{40}Ar/^{39}Ar$ age. The site of the FIB pit has an age of 276 ± 2 Ma which is within the expected age range. Fig. 6 shows age profiles on SW14-2 and MAD-2 trending away from the sites of FIB damage. For both samples, there is no systematic difference in age with distance from the FIB milled pit; all of the age values are within the expected range and lie within 2σ of each other. ^{36}Ar levels are low and show little variation throughout the FIB-milled area. In summary, the $^{40}Ar/^{39}Ar$ ages and ^{36}Ar abundances do not show any variation other than would be expected in a natural, unmodified sample, although the relatively large natural age variation in SW14 means that the impact of minor and highly localised FIB damage may be difficult to detect.

4.3. The effect of electron irradiation

Figs. 5 and 6 show the spatial distribution of $^{40}Ar/^{39}Ar$ age and ^{36}Ar in the slab fragments damaged by electron irradiation. Most of the ages in the SW14-2A subsample are within the expected range (261–281 Ma), apart from five analyses in the upper part of the field of view of the crystal. These analyses give younger than expected ages (as low as 249 Ma) and are from an area containing both pristine and deuterically altered feldspar. It is possible that these younger ages record post-cooling alteration and recrystallization, but in this case they would be expected to occur at the grain edge, where fluid flow is more likely to have taken place, or be associated with late stage veining. The youngest age (249 ± 2 Ma) occurs towards the centre of the crystal, and is not attributable to the presence of microcline veins because they are apparently absent from this sample. This area of younger ages is more than 100 μm away from the centre of electron beam damage and is adjacent to and overlaps with an area containing high levels of ^{36}Ar (Fig. 6). These high levels of ^{36}Ar are not exactly coincident with the electron damaged area, but occur 70 μm from the centre of electron damage in one direction only. A second area of electron damage was accidentally produced on

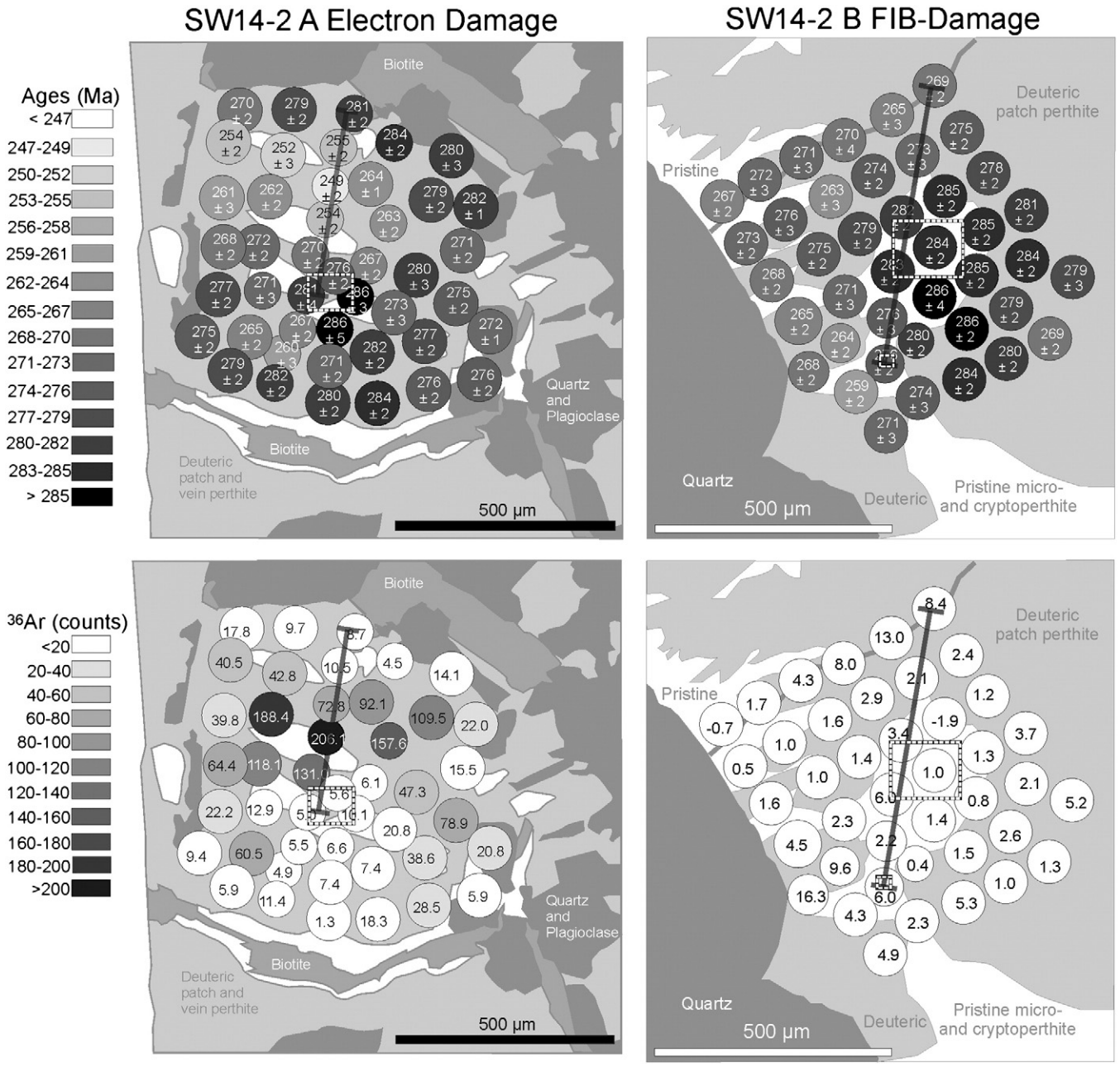

Fig. 5. Spatial distribution of $^{40}Ar/^{39}Ar$ age (a proxy for K and for $^{40}Ar^*$) and ^{36}Ar in SW14-2, with the locations of the FIB and electron beam damage. Ages are given with 1σ errors which include the propagated error on the J-value. The black lines give the position of the profiles shown in Fig. 6.

SW14-2B that underwent FIB-milling (Fig. 5); this was produced by normal high-resolution imaging of the feldspar crystal and was observable as a "burn" mark in CC-imaging. This area of damage occurs in the centre of a large area of pristine microtexture. It is associated with some of the oldest $^{40}Ar/^{39}Ar$ ages from this fragment, but these ages are nonetheless within the expected range and are unsurprising for a pristine region of feldspar. The ^{36}Ar values around this area of electron damage remain low. In MAD-2 the analyses around the area of electron damage gave the oldest ages from all three subsamples but this is likely due to the feldspar's natural age variation. There is no systematic variation in age with distance from the centre of electron beam damage and most ages are within 1 σ of each other. Most analyses gave ^{36}Ar levels within the expected range (<2 counts), but the analysis closest to the centre of electron damage gave the highest yield (8.8 ± 1.4 counts) of ^{36}Ar of all the analyses from the MAD subsamples. In summary, SW14-2A shows deviation from the expected values in both apparent $^{40}Ar/^{39}Ar$ age and ^{36}Ar yields with the maximum disturbance occurring 140–350 µm from the site of electron irradiation. MAD-2A shows a slight but noticeable increase in ^{36}Ar yield at the site of the electron irradiation.

4.4. The effect of HF etching

Age and ^{36}Ar maps for SW14-3 are given in the Supplementary data and the age and ^{36}Ar variation for SW14-3 and MAD-3 are listed in Table 1. The analyses from SW14-3 give the youngest average age of all of the Dartmoor fragments, but this is still within the expected range. The two youngest ages, however, are significantly younger than any of the ages produced by SW14-1. One of these young analyses also gave the highest ^{36}Ar yield from the fragment and five other analyses also gave higher than expected ^{36}Ar yields, but these are not associated with particularly young ages. MAD-3 produced significantly

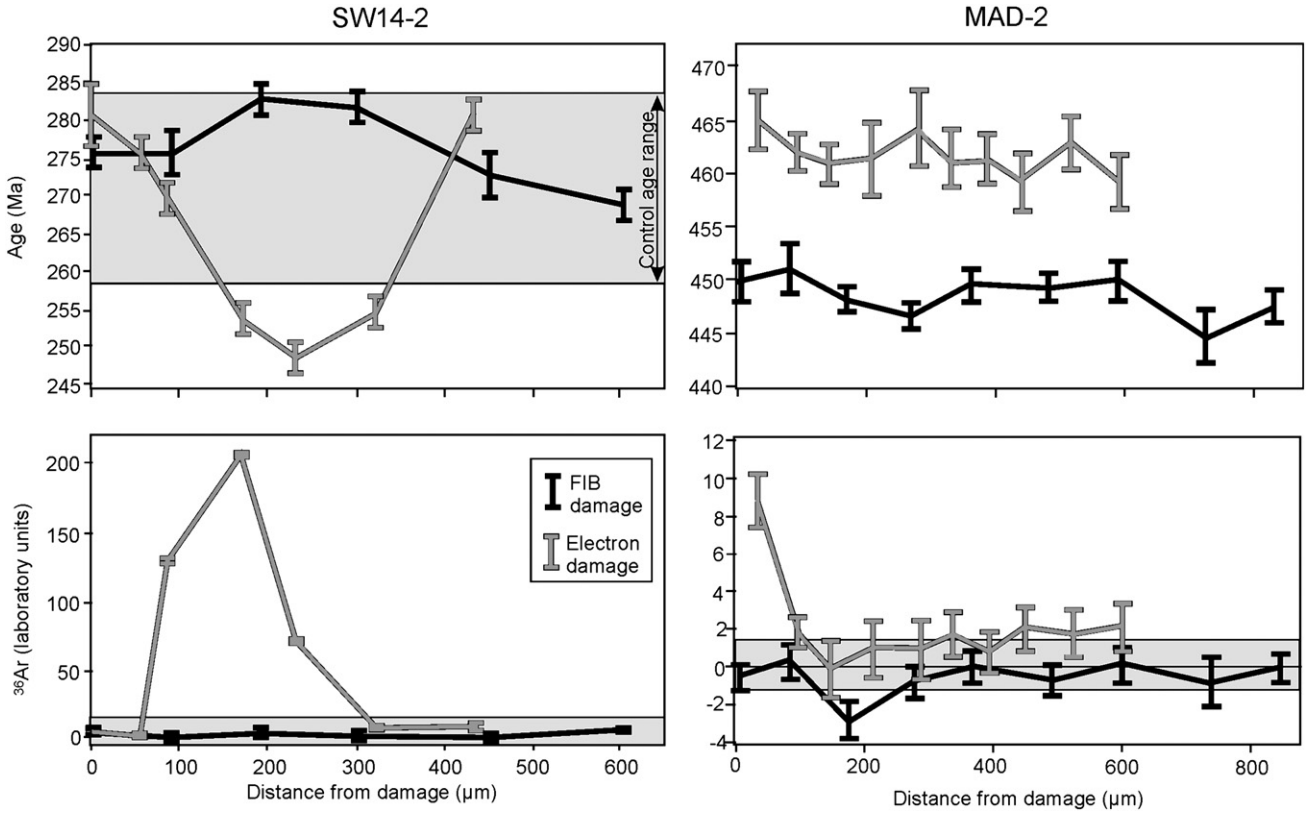

Fig. 6. Profiles of $^{40}Ar/^{39}Ar$ age and ^{36}Ar abundance with distance from the centre of FIB or electron beam damage.

higher ages than MAD-1, but as previously discussed these are likely due to natural age variation within the sample. The ^{36}Ar abundances from MAD-3 are low (less than 2 counts, and often indistinguishable from blank). In summary, sample MAD-3 showed no deviation from expected values, while parts of SW14-3 give younger apparent ages and higher ^{36}Ar yields than expected.

5. Discussion

The similarity of hydrocarbon and Cl abundances in instrument blank, control and irradiated samples suggests that no significant hydrocarbon or Cl contamination was introduced to the sample during SEM analysis and FIB-milling, or that any contamination introduced was easily removed by the gettering system on the extraction line attached to the Open University's Nu Instruments Noblesse mass spectrometer.

The data from the FIB damaged areas show no anomalous behaviour in age or ^{36}Ar yield, suggesting that the FIB milling process does not affect the $^{40}Ar/^{39}Ar$ system. The lack of disturbance to the FIB damaged areas also suggests that neither polishing with colloidal silica, nor rapid, low magnification SEM imaging causes significant disturbance to the $^{40}Ar/^{39}Ar$ system.

Areas of feldspar that underwent extreme electron beam damage show anomalous Ar-isotopic behaviour, which is more pronounced in SW14-2A, the microtexturally complex feldspar, than in the homogenous MAD-2A. Both samples have regions of increased ^{36}Ar yields and SW14-2A produced anomalously young ages. If an excess of ^{36}Ar were added to the sample, perhaps by the addition of fractionated atmospheric Ar, the apparent $^{40}Ar/^{39}Ar$ age would decrease due to overcorrection of atmospheric ^{40}Ar. While some of the younger ages are associated with high (>20 counts) ^{36}Ar, this is not always the case. Furthermore, some of the highest levels of ^{36}Ar are found in areas with a $^{40}Ar/^{39}Ar$ age indistinguishable from the control sample. It seems that the processes resulting in younger $^{40}Ar/^{39}Ar$ ages and higher levels of ^{36}Ar are not necessarily coupled, and that the anomalously young ages cannot be explained simply by the addition of ^{36}Ar. Plotting the SW14 data on an isotope correlation diagram shows that many of the elevated levels of ^{36}Ar in the electron damaged and etched subsamples can be easily explained by the addition of atmospheric Ar. The data from analysis SW14-1 spot 73, which gave a low ^{36}Ar yield, was used as a starting composition and the evolution of its isotopic composition with the addition of atmospheric Ar was modelled (black line, Fig. 7). Much of the scatter around this sample–atmosphere mixing line may be explained by different $^{40}Ar^*/^{39}Ar$ starting compositions, which result from different $^{40}Ar^*$ retentivities in diffusion domains of different sizes. However, closer examination of the isotope correlation diagram reveals an apparent array of data (grey triangles, Fig. 7) which forms a trend with a different gradient to the atmospheric mixing line. Extrapolating this line to both axes would give a higher than expected $^{39}Ar/^{40}Ar$ value, which is equivalent to a younger apparent age, and a lower $^{36}Ar/^{40}Ar$ value, which is often indicative of the presence of excess ^{40}Ar (albeit with a poor correlation, thus we refrain from quoting precise intercept values). Obviously, younger ages cannot be reconciled with excess ^{40}Ar, so if this data array is real then it represents disturbance to the Ar-isotope and K/Ar systems. This array is formed from data with a range of ages and ^{36}Ar yields, but each data point shows significant disturbance in at least one of these parameters (*i.e.* either high ^{36}Ar yields, low ages or both), observations which also indicate disturbance to the isotopic system. The trend of the array can be modelled (Fig. 7) by the addition of inversely proportional amounts of atmospheric Ar and K (as ^{39}Ar) to a model starting composition the same as SW14-1 spot 73. The additional K forms between 3% and 12% of the total ^{39}Ar while the additional atmospheric ^{40}Ar makes up 16–24% of the ^{40}Ar yield. Assuming a starting feldspar composition of 16.25 wt.% K_2O (Flude et al., 2012), the areas of feldspar that experienced the addition of K would yield an increase in K concentrations from 13.49 wt.% to between 13.9 and 15.1 wt.%. However, the patch

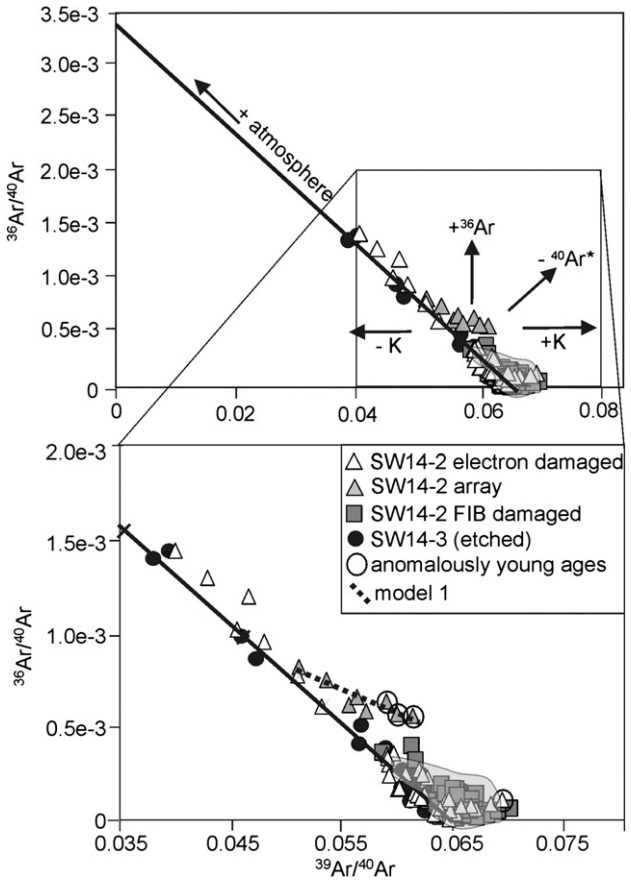

Fig. 7. Ar-isotope correlation diagram showing the SW14 data and expected behaviour with different scenarios for disturbance of the $^{40}Ar/^{39}Ar$ system. The box in the upper diagram represents the view of the lower diagram which is expanded to better show the data. Many of the data points associated with high ^{36}Ar yields can be modelled simply by the addition of atmospheric Ar. Eight of the data points from the area that was damaged by the electron beam appear to fall on an array, which can be modelled by the addition of ^{39}Ar (K) and atmospheric Ar.

perthites in the Dartmoor feldspars contain veins of Ab-rich feldspar which contain an average of just 0.16% K_2O. If the highest degrees of K-enrichment took place by migration of K from Or-rich areas to Ab-rich areas then a K flux of just 0.02 wt.% is required. The modelled trend is shown in Fig. 7 and the model data and calculations are given in the Supplementary data set. A closer look at the lower ^{36}Ar data from the electron damaged fragment reveals another possible array extending horizontally to the right of the diagram. The data from this array are indistinguishable from the data of the control sample, but trend towards an analysis that produced a particularly young age (249 Ma) and this second array can also be modelled by adding the same proportions of K as above but without the addition of atmospheric Ar.

It at first seems surprising that irradiation with 20 keV electrons damages the sample to a greater extent that 30 keV Ga^+ ions; Ga^+ ions are both higher energy and mass, so are more likely than an electron to cause physical damage to the sample. During irradiation with Ga^+ ions, the sample emits secondary electrons, which are used to form an image, but as the ion beam is formed from cations, rather than electrons, the sample is less likely to experience the extensive charging associated with SEM techniques. The disequilibrium behaviour of K within the electron damaged fragment implies that charging and electromigration of K play an important role in disturbing the K/Ar system. Presumably, K^+ becomes decoupled from the crystal lattice and migrates to areas where there is an excess of negative charge. The depth of the negatively charged layer formed during SEM work corresponds to the penetration depth of incident electrons (Toth et al., 2003), which in turn depends on the energy of the electron beam and the nature of the sample. According to the Kanaya–Okoyama equation (Kanaya and Okayama, 1972; Reed, 2005), 20 keV electrons would penetrate ~5.5 μm into a sample of alkali feldspar. This is a greater estimate than the 3–4 μm penetration depth suggested by Monte Carlo simulations (Fig. 1A), but is still shallower than the depth sampled during UV-LAMP $^{40}Ar/^{39}Ar$ analysis. The depth of the laser ablation pits was not determined for the present study, but is thought to be between 10 and 30 μm, based on previous laser ablation studies (Reddy et al., 1999, 2001; Wartho et al., 1999). For the shallowest ablation pits, up to 50% of the ablated volume may have experienced direct interaction with the electron beam during SEM analysis. However, the large distance (up to 400 μm) between the site of electron damage and the regions with greatest disturbance is puzzling as the sample–electron interaction volume is much smaller than the distance between these two sites, and thus the mechanism by which K^+ ions could migrate across such large distances is unclear.

The aim of this experiment was to empirically establish whether SEM techniques have the capacity to disturb the $^{40}Ar/^{39}Ar$ system in alkali feldspars and so determine whether it is viable to carry out *in-situ* UV-LAMP $^{40}Ar/^{39}Ar$ analysis on feldspar slabs that have been previously microtexturally characterised using SEM techniques. While the results are surprising, a detailed analysis of the mechanism of this disturbance is outside the scope of this study due to a lack of appropriate experimental data, and we encourage others to try and reproduce and investigate this phenomenon. However, recent papers studying alkali migration in electron irradiated glasses allow us to speculate on possible mechanisms and, importantly, corroborate the surprisingly large distances of K-migration suggested by our results. Jurek and Gedeon (2008) electron-irradiated carbon coated, alkali-bearing glasses for 3 and 5 days using a 60 μm diameter, 50 keV beam with a current of 50 nA in a JEOL JXA 733 electron microprobe. They subsequently analysed the glass by EMPA with an ED spectrometer at different depths by varying the beam energy between 10 and 30 keV and using a moderate current of <1 nA. They observed lateral depletion of K up to 100 μm from the centre of the irradiated area and at up to 25 μm below the irradiated sample surface, which is well below the calculated electron penetration depth. The K-depletion was most pronounced at the surface and decreased with depth and distance from the centre of irradiation. Their study confirms that migration of K during electron irradiation over 100 μm length scales is possible and does occur. In one of their experiments, they noted a slight accumulation of K in the point analysis furthest from the centre of irradiation, but apparently did not analyse the glass at greater distances and did not investigate where the K had migrated to, presumably assuming that it had migrated downwards into the bulk of the sample, where it was below the interaction volume of the EMPA technique employed. Their observation of K-migration at depths up to 25 μm below the irradiated surface also suggests that up to 100% of the volume of material analysed by UV-LAMP $^{40}Ar/^{39}Ar$ analysis in our study may have undergone K-migration. A second study by Gedeon et al. (2009) first irradiated a carbon-coated 7 mm thick slab of glass with high energy (2.5 MeV) electrons, which were calculated to penetrate into the sample to a depth slightly less than the sample thickness, and subsequently irradiated spots on both the top and bottom surface of the slab using 50 keV electrons. They observed greater mobility of K and greater degree of structural change to the glass in the spot on the bottom surface of the slab — *i.e.* in the region directly below the interaction volume of the first irradiation. They interpreted these results in terms of a greater degree of structural damage to the glass near the base of the slab during the initial irradiation, due to a steady flow of slow electrons out of the bottom of the interaction volume. In their experiment, the bottom of the slab was also carbon-coated and grounded, so an intense

electrical field would have developed between the base of the negatively charged layer and the grounded surface. Such conditions were not employed during electron irradiation of our samples, but it may be that structural damage to the region below the irradiated volume is more common than previously recognised, and can promote faster K-migration at depth during subsequent or prolonged irradiation.

The Jurek and Gedeon (2008) irradiation experiments were carried out over much longer time periods than our own, but their samples were carbon-coated and grounded, and it is unclear how a lack of conductive coating may affect the electrical field that forms during irradiation; it may be that the higher degree of charging that occurs in a sample due to the lack of a carbon-coat results in similar processes occurring at faster rates. Furthermore, Flude et al. (2012) noted that areas of feldspar that were CC imaged at high magnification retained a higher secondary electron emission at lower magnification, and such areas may persist even if the sample is removed from the SEM and imaged at a later date, indicating a combination of changes to the feldspar structure that enhance charging (*i.e.* development of more charge traps) and retention of charge in the sample. This indicates that regions of negative charge may be retained in the sample, even when it is no longer experiencing electron irradiation, at least on the scale of minutes to hours, effectively increasing the time during which K is able to migrate.

Differences in Ar-isotopic behaviour between irradiated perthitic (SW14) and gem-quality (MAD) samples may be explained by different charging behaviours due to the contrasting microtextures in the two samples. During CC imaging of perthitic phenocrysts from the Dartmoor Granite (Flude et al., 2012) both the Ab-rich and irregular microcline subgrains in patch perthites exhibited a higher intensity of secondary electron emission than surrounding tweed orthoclase, indicating a greater degree of charging and charge trapping due to differences in their chemical composition and/or lattice defect densities, suggesting that albite and irregular microcline are more prone to charging than tweed orthoclase. Furthermore, the intimate intergrowth of Ab- and Or-rich feldspar in patch perthites means that any migration of K within the grain may result in significant local compositional changes. This suggests that patch perthites are much more susceptible to damage during electron irradiation than pristine and gem quality feldspars and this is consistent with our observations that sample SW14 experienced greater damage during electron irradiation than sample MAD. It may also explain the lack of disturbance associated with the "burn mark" on sample SW14-2B as it was centred on a relatively large area of pristine feldspar composed of coherent microperthite and cryptoperthite. However, we acknowledge that the lack of disturbance may also be due to the SW14-2B burn mark being produced by a shorter irradiation time than that experienced by SW14-2A.

The incorporation of atmospheric Ar into the sample is unlikely to have occurred by diffusion, as the calculated temperatures during electron irradiation are insufficiently high, and in any case this would be accompanied by diffusive loss of $^{40}Ar^*$, which was not recorded. The disturbed data array can also be modelled by the inversely proportional addition of atmospheric Ar and removal of $^{40}Ar^*$ (see Supplementary data) so that up to 11% $^{40}Ar^*$ is lost from the sample. In this case the greatest addition of atmospheric Ar is associated with the smallest loss of $^{40}Ar^*$, which would not be the case if the gain and loss of Ar was due to diffusion. We note that the same effect may be produced by the addition of fractionated atmospheric Ar, with a $^{40}Ar/^{36}Ar$ value greater than 298.56, but if this were the case the disturbed data array (Fig. 7) would have an intercept indicating an excess of ^{36}Ar, rather than the apparent excess of ^{40}Ar that is observed. It may be that naturally occurring defects and dislocations are enhanced and opened to the sample surface during electron irradiation, allowing atmospheric Ar to become adhered to these new surfaces. Alternatively, Ar in the microscope chamber may become positively charged by the electron beam and become implanted on the sample during charge neutralisation at the sample surface. This process may explain the modelled inverse proportionality between gain of K and atmospheric Ar, as addition of K^+ ions will begin to neutralise negative charge in that region of the sample, resulting in reduced secondary electron emission, thus reduced attraction of positive ions within the microscope chamber. In the homogenous MAD sample, the region of greatest charging at the surface would be the site of impact of the electron beam, which is where the increase in atmospheric Ar is observed, while in the SW14 sample, charging is dependent on the structure and characteristics of the feldspar microtextures and is variable across the sample. An interesting experiment would be to carry out the same SEM procedures using coated samples under vacuum, or using an environmental SEM with nitrogen gas in the sample chamber to see whether the addition of atmospheric Ar still takes place.

In SW14, the area of electron-disturbance to the $^{40}Ar/^{39}Ar$ system is not radially arranged around the irradiation site, as might be expected. The reasons for this are unknown, but sample inhomogeneity probably plays a role. Alternatively, electron irradiation and imaging of the crystal before and after the 8 minute irradiation may have resulted in the development of a network of charging and migration pathways which then promoted K-migration in a particular direction. This outcome was not anticipated during the experimental design, and so the appropriate observations with which to test this were not made.

The high ^{36}Ar analyses from SW14-3 lie along the atmospheric mixing line discussed previously and shown in Fig. 7, suggesting that the elevated ^{36}Ar levels are due to the addition of atmospheric Ar. The two youngest ages lie just to the right of this line and so may represent some loss of $^{40}Ar^*$ or gain of K. These effects may be related to the HF etching, which is unexpected because many $^{40}Ar/^{39}Ar$ labs routinely etch volcanic feldspars in HF to improve data quality. However, volcanic alkali feldspars typically lack strain-controlled and deuteric microperthites, and so may be less susceptible to disturbance of the $^{40}Ar/^{39}Ar$ system. Alternatively, the young ages and high levels of ^{36}Ar may result from natural alteration; this fragment was broken along a cleavage plane, which may have already acted as a conduit for fluid flow causing alteration of the feldspar. We recommend that further work is carried out to investigate the effects of HF etching on the $^{40}Ar/^{39}Ar$ systematics of feldspars and other minerals, if this process is to be used routinely.

6. Summary and conclusions

Techniques used to characterise feldspar microtextures, including EMPA, EBSD mapping, OC and CC imaging, may disturb the $^{40}Ar/^{39}Ar$ system and so may lead to erroneous ages if applied to the same area of the same sample to be used for $^{40}Ar/^{39}Ar$ dating. While contamination with hydrocarbons and Cl does not seem to cause a problem, sample charging during SEM work can cause addition of atmospheric Ar and redistribution of K within the sample. Sample damage increases with microtextural complexity, can occur at hundreds of micrometres from the electron irradiation site, and is most probably caused by the accumulation of negative charge in the sample. Short duration and low-resolution SEM imaging of feldspar slabs to be used for $^{40}Ar/^{39}Ar$ analysis does not necessarily cause significant disturbance to the $^{40}Ar/^{39}Ar$ system, but we suggest any such work should be carried out on coated samples to reduce sample charging, that leaving the sample under the electron beam for extended periods of time should be avoided, as should imaging at high magnification, and that the users be aware of the potential for sample damage using these techniques. Polishing with colloidal silica does not seem to affect the $^{40}Ar/^{39}Ar$ system, but etching with HF may add atmospheric Ar to the sample.

Acknowledgements

James Schwanethal (CEPSAR, Open University, now London Geochronology Centre, Birkbeck) is thanked for assistance in the $^{40}Ar/^{39}Ar$ lab. We thank Peter Chung (School of Geographical and

Earth Sciences, University of Glasgow) for help with the SEM work and Billy Smith (School of Physics and Astronomy, University of Glasgow) for assistance with the FIB work. Two anonymous reviewers are thanked for their comments along with editor Klaus Mezger. This work was funded by NERC grant NE/E018629/1.

Appendix A. Supplementary data

Supplementary data to this article can be found online at http://dx.doi.org/10.1016/j.chemgeo.2013.07.003.

References

Arnaud, N.O., Kelley, S.P., 1997. Argon behaviour in gem-quality orthoclase from Madagascar: experiments and some consequences for $^{40}Ar/^{39}Ar$ geochronology. Geochimica et Cosmochimica Acta 61, 3227–3255.

Autefage, F., 1980. Variations de la teneur en sodium et en potassium dans des mineraux au cours de leur analyse a la microsonde electronique (Variations in the concentrations of sodium and potassium during their analysis with the electron microprobe). Bulletin de Mineralogie 103, 48–53.

Cahill, D., Watson, S., Pohl, R., 1992. Lower limit to the thermal conductivity of disordered crystals. Physical Review B 46, 6131–6140.

Cazaux, J., 1986. Some considerations on the electric field induced in insulators by electron bombardment. Journal of Applied Physics 59, 1418.

Cazaux, J., 1996. Electron probe microanalysis of insulating materials: quantification problems and some possible solutions. X-Ray Spectrometry 25, 265–280.

Chesley, J.T., Halliday, A.N., Snee, L.W., Mezger, K., Shepherd, T.J., Scrivener, R.C., 1993. Thermochronology of the Cornubian batholith in southwest England: implications for pluton emplacement and protracted hydrothermal mineralization. Geochimica et Cosmochimica Acta 57, 1817–1835.

Egerton, R.F., Li, P., Malac, M., 2004. Radiation damage in the TEM and SEM. Micron 35, 399–409.

Flude, S., Lee, M.R., Sherlock, S.C., Kelley, S.P., 2012. Cryptic microtextures and geological histories of K-rich alkali feldspars revealed by charge contrast imaging. Contributions to Mineralogy and Petrology 163, 983–994.

Flude, S., Halton, A., Kelley, S.P., Sherlock, S.C., Schwanethal, J., Wilkinson, C., under review. Observation of centimetre scale argon diffusion in alkali feldspars: implications for $^{40}Ar/^{39}Ar$ thermochronology.

Gedeon, O., Liška, M., 2001. Molecular dynamic modelling of potassium transport in a potassium-silicate glass irradiated by fast electrons. Journal of Non-Crystalline Solids 286, 181–186.

Gedeon, O., Jurek, K., Huĺınský, V., 1999. Fast migration of alkali ions in glass irradiated by electrons. Journal of Non-Crystalline Solids 246, 1–8.

Gedeon, O., Zemek, J., Jurek, K., 2008. Changes in alkali-silicate glasses induced with electron irradiation. Journal of Non-Crystalline Solids 354, 1169–1171.

Gedeon, O., Jurek, K., Drbohlav, I., Ollier, N., 2009. Binary potassium-silicate glass irradiated with electrons. Nuclear Instruments and Methods in Physics Research Section B: Beam Interactions with Materials and Atoms 267, 3461–3465.

Harrison, T. Mark, Heizler, Matthew T., McKeegan, Kevin D., Schmitt, Axel K., 2010. *In-situ* $^{40}K–^{40}Ca$ 'double-plus' SIMS Dating Resolves Klokken Feldspar $^{40}K–^{40}Ar$ Paradox. Earth and Planetary Science Letters 299 (3–4), 426–433. http://dx.doi.org/10.1016/j.epsl.2010.09.023 (November 1).

Höfer, M., Schilling, F.R., 2002. Heat transfer in quartz, orthoclase, and sanding at elevated temperature. Physics and Chemistry of Minerals 29, 571–584.

Jiang, N., Silcox, J., 2002. Electron irradiation induced phase decomposition in alkaline earth multi-component oxide glass. Journal of Applied Physics 92, 2310.

Jourdan, F., Matzel, J.P., Renne, P.R., 2007. ^{39}Ar and ^{37}Ar recoil loss during neutron irradiation of sanidine and plagioclase. Geochimica et Cosmochimica Acta 71, 2791–2808.

Jurek, K., Gedeon, O., 2008. Volume and composition surface changes in alkali silicate glass irradiated with electrons. Microchimica Acta 161, 377–380.

Kanaya, K., Okayama, S., 1972. Penetration and energy-loss theory of electrons in solid targets. Journal of Physics D: Applied Physics 5, 43–58.

Lee, M.R., 2010. Transmission electron microscopy (TEM) of Earth and planetary materials: a review. Mineralogical Magazine 74, 1–27.

Lee, M.R., Waldron, K.A., Parsons, I., 1995. Exsolution and alteration microtextures in alkali feldspar phenocrysts from the Shap Granite. Mineralogical Magazine 59, 63–78.

Lee, J.-Y., Marti, K., Severinghaus, J.P., Kawamura, K., Yoo, H.-S., Lee, J.B., Kim, J.S., 2006. A redetermination of the isotopic abundances of atmospheric Ar. Geochimica et Cosmochimica Acta 70, 4507–4512.

Lee, M.R., Brown, D.J., Smith, C.L., Hodson, M.E., MacKenzie, M., Hellmann, R., 2007. Characterization of mineral surfaces using FIB and TEM: a case study of naturally weathered alkali feldspars. American Mineralogist 92, 1383–1394.

Lineweaver, J.L., 1963. Oxygen outgassing caused by electron bombardment of glass. Journal of Applied Physics 34, 1786.

Lovera, O.M., Richter, F.M., Harrison, T.M., 1989. The $^{40}Ar/^{39}Ar$ thermochronometry for slowly cooled samples having a distribution of diffusion domain sizes. Journal of Geophysical Research 94 (B12), 17917–17935.

Lovera, O.M., Grove, M., Harrison, T.M., 2002. Systematic analysis of K-feldspar $^{40}Ar/^{39}Ar$ step heating results II: relevance of laboratory argon diffusion properties to nature. Geochimica et Cosmochimica Acta 66, 1237–1255.

Mark, D.F., Kelley, S.P., Lee, M.R., Parnell, J., Sherlock, S.C., Brown, D.J., 2008. Ar–Ar dating of authigenic K-feldspar: quantitative modelling of radiogenic argon-loss through subgrain boundary networks. Geochimica et Cosmochimica Acta 72, 2695–2710.

McConnell, J.D.C., 1969. Photochemical degradation of a silicate in the beam of the electron microscope. Philosophical Magazine 20, 1195–1202.

McDougall, I., Harrison, T.M., 1999. Geochronology and Thermochronology by the $^{40}Ar/^{39}Ar$ Method, 2nd ed. Oxford University Press.

McDougall, Ian, Wellman, Peter, 2011. Calibration of GA1550 Biotite Standard for K/Ar and $^{40}Ar/^{39}Ar$ dating. Chemical Geology 280 (1–2), 19–25. http://dx.doi.org/10.1016/j.chemgeo.2010.10.001 (January 7).

McLaren, S., Reddy, S.M., 2008. Automated mapping of K-feldspar by electron backscatter diffraction and application to $^{40}Ar/^{39}Ar$ dating. Journal of Structural Geology 30, 1229–1241.

McLaren, S., Dunlap, W.J., Powell, R., 2007. Understanding K-feldspar $^{40}Ar/^{39}Ar$ data: reconciling models, methods and microtextures. Journal of the Geological Society 164, 941–944.

Nägler, Th.F., Villa, I.M., 2000. In pursuit of the ^{40}K branching ratios: K–Ca and $^{39}Ar–^{40}Ar$ dating of gem silicates. Chemical Geology 169 (1–2), 5–16. http://dx.doi.org/10.1016/S0009-2541(99)00194-1 (August 15).

Nielsen, C.H., Sigurdsson, H., 1981. Quantitative methods for electron microprobe analysis of sodium in natural and synthetic glasses. American Mineralogist 66, 547–552.

Parsons, I., Rex, D.C., Guise, P., Halliday, A.N., 1988. Argon-loss by alkali feldspars. Geochimica et Cosmochimica Acta 52, 1097–1112.

Parsons, I., Brown, W.L., Smith, J.V., 1999. $^{40}Ar/^{39}Ar$ thermochronology using alkali feldspars: real thermal history or mathematical mirage of microtexture? Contributions to Mineralogy and Petrology 136, 92–110.

Pertermann, M., Whittington, A.G., Hofmeister, A.M., Spera, F.J., Zayak, J., 2007. Transport properties of low-sanidine single-crystals, glasses and melts at high temperature. Contributions to Mineralogy and Petrology 155, 689–702.

Prenitzer, B.I., Urbanik-Shannon, C.A., Giannuzzi, L.A., Brown, S.R., Irwin, R.B., Shofner, T.L., Stevie, F.A., 2003. The correlation between ion beam/material interactions and practical FIB specimen preparation. Microscopy and Microanalysis 9, 216–236.

Prior, D.J., Boyle, A.P., Brenker, F., Cheadle, M.C., Day, A., Lopez, G., Peruzzi, L., Potts, G., Reddy, S., Spiess, R., Timms, N.E., Trimby, P., Wheeler, J., Zetterstrom, L., 1999. The application of electron backscatter diffraction and orientation contrast imaging in the SEM to textural problems in rocks. American Mineralogist 84, 1741–1759.

Reddy, S.M., Potts, G.J., Kelley, S.P., Arnaud, N.O., 1999. The effects of deformation-induced microstructures on intragrain $^{40}Ar/^{39}Ar$ ages in potassium feldspar. Geology 27, 363–366.

Reddy, S.M., Potts, G.J., Kelley, S.P., 2001. $^{40}Ar/^{39}Ar$ ages in deformed potassium feldspar: evidence of microstructural control on Ar isotope systematics. Contributions to Mineralogy and Petrology 141, 186–200.

Reed, S.J.B., 2005. Electron Microprobe Analysis and Scanning Electron Microscopy in Geology, 2nd ed.

Renne, Paul R., Swisher, Carl C., Deino, Alan L., Karner, Daniel B., Owens, Thomas L., DePaolo, Donald J., 1998. Intercalibration of standards, absolute ages and uncertainties in $^{40}Ar/^{39}Ar$ dating. Chemical Geology 145 (1–2), 117–152. http://dx.doi.org/10.1016/S0009-2541(97)00159-9 (March 6).

Richter, F.M., Lovera, O.M., Mark Harrison, T., Copeland, P., 1991. Tibetan tectonics from $^{40}Ar/^{39}Ar$ analysis of a single K-feldspar sample. Earth and Planetary Science Letters 105, 266–278.

Sass, J.H., 1965. The thermal conductivity of fifteen feldspar specimens. Journal of Geophysical Research 70, 4064–4065.

Schwarz, Winfried H., Trieloff, Mario, 2007. Intercalibration of $^{40}Ar–^{39}Ar$ Age standards NL-25, HB3gr hornblende, GA1550, SB-3, HD-B1 biotite and BMus/2 muscovite. Chemical Geology 242 (1–2), 218–231. http://dx.doi.org/10.1016/j.chemgeo.2007.03.016 (July 30).

Smith, J.V., Brown, W.L., 1988. Feldspar Minerals, vol. 1. Springer-Verlag, Berlin.

Smith, C.L., Lee, M.R., MacKenzie, M., 2006. New opportunities for nanomineralogy using FIB, STEM/EDX and TEM. Microscopy and Analysis 20, 17–20.

Spell, T., McDougall, I., 2003. Characterization and calibration of $^{40}Ar/^{39}Ar$ dating standards. Chemical Geology 198 (3–4), 189–211. http://dx.doi.org/10.1016/S0009-2541(03)00005-6 (August 15).

Spray, J.G., Rae, D.A., 1995. Quantitative electron-microprobe analysis of alkali silicate glasses: a review and user guide. Canadian Mineralogist 33, 323–332.

Sweatman, T.R., Long, J.V.P., 1969. Quantitative electron-probe microanalysis of rock-forming minerals. Journal of Petrology 10, 332–379.

Toth, M., Thiel, B.L., Donald, A.M., 2003. Interpretation of secondary electron images obtained using a low vacuum SEM. Ultramicroscopy 94, 71–87.

Villa, Igor M., 2006. From nanometer to megameter: isotopes, atomic-scale processes, and continent-scale tectonic models. Lithos 87 (3–4), 155–173. http://dx.doi.org/10.1016/j.lithos.2005.06.012 (April).

Villa, Igor M., Hanchar, John M., 2013. K-feldspar hygrochronology. Geochimica et Cosmochimica Acta 101, 24–33. http://dx.doi.org/10.1016/j.gca.2012.09.047 (January).

Villa, Igor M., Ruggieri, Giovanni, Puxeddu, Mariano, Bertini, Giovanni, 2006. Geochronology and isotope transport systematics in a subsurface granite from the Larderello–Travale geothermal system (Italy). Journal of Volcanology and Geothermal Research 152 (1–2), 20–50. http://dx.doi.org/10.1016/j.jvolgeores.2005.09.011 (April).

Wartho, J.-A., Kelley, S.P., Brooker, R.A., Carroll, M.R., Villa, I.M., Lee, M.R., 1999. Direct measurement of Ar diffusion profiles in a gem-quality Madagascar K-feldspar using the ultra-violet laser ablation microprobe (UVLAMP). Earth and Planetary Science Letters 170, 141–153.

Wirth, R., 2009. Focused ion beam (FIB) combined with SEM and TEM: advanced analytical tools for studies of chemical composition, microstructure and crystal structure in geomaterials on a nanometre scale. Chemical Geology 261, 217–229.